Fluid-body interactions: clashing, skimming, bouncing

Frank T. Smith*& Phillip L. Wilson†

January 11, 2011

Abstract

Solid-solid and solid-fluid impacts and bouncing are the concern here. A theoretical study is presented on fluid-body interaction in which the motion of the body and the fluid influence each other nonlinearly. There could also be many bodies involved. The clashing refers to solid-solid impact arising from fluid-body interaction in a channel, while the skimming refers to another area where a thin body impacts obliquely upon a fluid surface. Bouncing usually then follows in both areas. The main new contribution concerns the influences of thickness and camber which lead to a different and more general form of clashing and hence bouncing.

Index words: fluid-body interaction; clashing; skimming; bouncing.

1 Introduction

The present motivation, apart from much intrinsic interest in the subject of free body movement within a fluid in general, is from industrial, biomedical and sports applications and other arenas. The industrial applications are manyfold including in particular ship slamming, sloshing and granular flows on chutes [1–20]. There is also a huge number of biomedical applications [21–31], while sports applications are such as in skeleton bobsleigh. The work is on fluid-body interaction [32]. The article is aimed mostly at analytical understanding and results.

The present contribution is based on two recent findings and one new piece of work, with bouncing or rebounding being a common feature. The first is [32] where interactions between a finite number of moving bodies and the surrounding fluid in a channel are investigated. The bodies or grains are thin, straight and free to move in a nearly parallel configuration in quasiinviscid fluid, the combined motion being assumed to be planar for modelling purposes. Numerical and analytical aspects are presented. Three major features appear, namely an instability about the uniform state, a solid-to-solid clashing (body-wall or body-body) within a finite time, and a continuum limit for many bodies. The finding of most interest here is that of clashing. Second is the theoretical investigation by [33] of the evolution for the combined solid-fluid motion when a solid body undergoes a skimming impact with and possibly rebounds from a shallow liquid layer, *e.g.* shallow-water skipping. Depending on the parameter range involved the induced lift on the body due to flow pressure is sufficient to entirely retard the incident downward motion before causing the body to exit from the layer within a finite scaled time. The work with almost exactly the same interaction structure as in the first study thus yields skimming, lift-off from the water and subsequent bouncing. Third, the new piece here is on the unsteady interactions between a body and the fluid flowing past it, inside a channel again but with a more realistic body. Indeed, the study [32] by Smith & Ellis is for one or more infinitesimally thin plates in inviscid fluid, whereas the current investigation is also for a (quasi) inviscid incompressible fluid but the contained moving body has thickness and camber. These turn out to be important features.

Section 2 below describes the interactive body-fluid configuration, formulation and main properties of the numerical solutions obtained for the nonlinear setting with a single body having thickness and/or camber. All cases are found to yield a solid-solid clash within a finite

*Department of Mathematics, UCL, Gower Street, London WC1E 6BT, UK. frank@math.ucl.ac.uk

†Department of Mathematics & Statistics, University of Canterbury, Private Bag 4800, Christchurch 8140, New Zealand.

scaled time. This can be contrasted and compared with the interesting findings of [19, 34–42]. The typical present clash occurs mid-body instead of at the leading edge as in [32] and this new form is examined in detail in sections 3, 4. Comparisons between the numerical results and the clash analysis are in section 5. Section 6 presents final comments.

2 Configuration and solution properties

The focus is on a single body as in figure 1. In terms of the formulation and methodology the body-fluid interaction takes place inside a slender channel in a two-dimensional $x-y$ plane where x, y are Cartesian coordinates non-dimensionalised with respect to a representative longitudinal length L^*. The body or grain is thin but with nonzero thickness or camber (or both) and with its angles of inclination during motion being of the same small order b, say, as those of the containing channel. The typical flow speed over the time scales of concern is U^*, with the (x, y) velocity components (u, v), pressure variation p, and time t being based on U^*, $\rho^* U^{*2}$, and L^*/H^* respectively, where ρ^* is the fluid density. The representative length scale for x is of order unity by definition, whereas that for y is b; similarly, u is of $O(1)$ whereas v is of $O(b)$ by continuity, and p, t are typically of $O(1)$. For convenience we write $y = bY$ and $v = bV$, so that Y lies between 0 and 1. Also the quantity Reb^2 is supposed to be large, meaning that viscous effects are nominally negligible, with Re being the appropriate Reynolds number, while the effective Froude number is likewise taken to be large such that gravity effects are negligible. Two-way nonlinear interaction takes place simply because the fluid dynamical forces cause body movement which in turn affects the fluid motion.

The scales involved imply the governing equations

$$u_x + V_Y = 0 \tag{1a}$$

$$u_t + uu_x + Vu_Y = -p_x \tag{1b}$$

for each $u = u_n$, $V = V_n$, $p = p_n$ owing to continuity and streamwise momentum in the two thin layers present as in figure 1. The normal momentum balance yields $\partial p/\partial Y$ being zero at this level, so that $p(x, t)$ is independent of Y in each layer, in effect. The subscripts $n = 1, 2$ here and below refer to values within the two fluid layers on either side of the body. The range of x is from 0 to 1. The lateral boundary conditions are the kinematic ones

$$V = f_t + uf_x \text{ at } Y = f(x, t) \tag{2}$$

for each solid moving boundary at scaled position $Y = f$ (determined by a central position, a scaled thickness effect T, and a scaled camber C as specified later), acting together with the tangential flow conditions at the straight fixed walls,

$$V = 0 \text{ at } Y = 0, 1. \tag{3}$$

The oncoming flow has $(u, V, p) = (1, 0, 0)$ ahead of the leading edge position $x = 0$, generating the jump requirements

$$p_n + \frac{1}{2}u_n^2 = \frac{1}{2} \text{ at } x = 0+, \tag{4a}$$

$$\frac{\partial u_n}{\partial Y} = 0 \text{ at } x = 0+ \tag{4b}$$

in each gap as in [32]. The fluid flow equations in each gap now yield the shallow-water relations

$$H_t + (uH)_x = 0 \ , \tag{5a}$$

$$u_t + uu_x = -p_x \ , \tag{5b}$$

in view of (1)–(4), where the two unknown H values denote the scaled gap widths in the form

$$H_1(x, t) = h(t) + C(x) - \frac{1}{2}T(x) + (x - 1/2)\theta(t) \ , \tag{6a}$$

$$H_2(x, t) = 1 - h(t) - C(x) - \frac{1}{2}T(x) - (x - 1/2)\theta(t) \ , \tag{6b}$$

for definiteness, where camber and thickness are defined in figure 1. The total mass balance then requires

$$u_1 H_1 + u_2 H_2 = 1 \text{ at } x = 1- . \tag{7}$$

Also at the trailing edge $x = 1$ a Kutta condition holds, imposing on the fluid flow the constraint

$$p_1 = p_2 = \pi_e(t) \text{ at } x = 1- \tag{8}$$

with an unknown pressure value π_e which depends on t.

Along with the above the body itself moves mainly in response to the fluid dynamical pressure forces acting on the body surfaces. Thus since the unknown body position is that implied by (6a,b) the balances of lateral and angular motion require

$$M\ddot{h} = -\int (p_2 - p_1)\, dx \ , \tag{9a}$$

$$I\ddot{\theta} = -\int (x - \frac{1}{2})(p_2 - p_1)\, dx \ , \tag{9b}$$

respectively, where a dot represents differentiation with respect to t. Here, to clarify, h is the Y-position of the body centre of mass (the x-position being close to 1/2), θ is the angle of inclination of the body, while M, I are the scaled mass and moment of inertia in turn. (All numerical results presented herein take $M = 1 = I$.) The streamwise motion is dominated by the requirement of constant streamwise velocity of the body as the fluid dynamical forces are comparatively small in that direction.

The system of interest is therefore (4a), (5)–(9). Numerical solutions of this nonlinear system were obtained by finite differencing and iteration as in [32] with analytical treatments used as checks. An integrated form of (5a) proves advantageous here, giving

$$H_1 u_1 = c_1 - (x - \frac{1}{2})\dot{h} - \frac{1}{2}(x - \frac{1}{2})^2\dot{\theta} \ , \tag{10a}$$

$$H_2 u_2 = c_2 + (x - \frac{1}{2})\dot{h} + \frac{1}{2}(x - \frac{1}{2})^2\dot{\theta} \ , \tag{10b}$$

with the temporal functions of integration being constrained by

$$c_1(t) + c_2(t) = 1 \tag{11}$$

because of (7). Results are shown in figures 2, 3 for a number of particular cases. When the camber is zero but thickness varies, figure 2(a) shows that the early motion is dominated by a linear increase in θ. This is followed by a continuing growth of θ accompanied by motion towards the lower wall. The added-mass effect for larger variations in thickness accelerates the motion towards the wall. Figure 2(b) shows that flows can become negative in the closing gap between the body and the wall, and that the flows in both gaps show Bernoulli-like increases towards the centre of the body where the thickness is greatest. The clash in the $C(x) = 0 = T(x)$ case is occuring close to the leading edge, whereas in the remaining cases it appears to occur away from the leading and trailing edges in general, also in keeping with figure 5. When the thickness is zero but the camber varies, figure 3(a) suggests that the resulting lift-induced migration to the wall and angular acceleration affect the flow more strongly than in the zero camber cases. Figure 3(b) shows that, once again, flows can become negative in the closing gap, and Bernoulli-like effects are again seen as the concave-downwards body migrates to the wall. Again, clashes are occurring in general away from the leading and trailing edges. In all cases, leading- and trailing-edge velocity appears to approach a linear asymptote before the clash. Similar effects are to be expected for cases with camber and thickness both present.

Since the cases for which $C(x) = 0 = T(x)$ agree with those of [32], similar properties are to be expected for many bodies present, as in [32]. Clashing within a finite time is clearly suggested with the minimum of one of the gap widths approaching zero at an x-station away from the leading and trailing edges in general.

3 Finite-time clashes and local effects

The task now is to explain the mathematical structure of the fluid-body interaction as the clashing occurs, and in particular to elucidate the contributions of the local and non-local dynamics

which turn out to have similar degrees of importance. Also this analysis is in preparation for future study of the post-clash phase, *i.e.* the start of the rebound, subsequent interactive motion and so on, where an analogous solution structure is to be expected. The finite-time clashing is found analytically here to have a solution structure different from that in [32] which corresponded to perhaps rather gentle clashes happening at leading edges. Instead the typical clash is now centred mid-chord, as follows, with both local and global effects having significant roles.

Supposing the clash is centred near some $x = x_0$ with $0 < x_0 < 1$, and that the gap width H_1 first tends to zero there at a time $t = t_0$, we have locally H_1 to be of order $(t_0 - t)^n$, say, with the unknown power n being positive. The smooth local body shape then indicates that typically Y is of order $(x - x_0)^2$ and so the spatial scalings $(x - x_0) \sim (t_0 - t)^{\frac{n}{2}}$, $Y \sim H_1 \sim (t_0 - t)^n$ are inferred. An argument based on the consequent fluid velocities and hence pressure then leads through the added mass concept to the conclusion that n must be zero or unity on account of the equations of body motion (9a,b). The former value is contradictory; hence $n = 1$. The resulting asymptotic description therefore takes the form

$$h = h_{10} + (t_0 - t)h_{11} + (t_0 - t)^{\frac{3}{2}} h_{12} + \dots \ , \tag{12a}$$

$$\theta = \theta_{10} + (t_0 - t)\theta_{11} + (t_0 - t)^{\frac{3}{2}} \theta_{12} + \dots \ , \tag{12b}$$

$$c_1 = c_{11} + (t_0 - t)^{\frac{1}{2}} c_{12} + \dots \ , \tag{12c}$$

$$F_1 = F_{10} + (t_0 - t)^{\frac{1}{2}} \xi F_{11} + (t_0 - t)\xi^2 F_{12} + \dots \ , \tag{12d}$$

for $t \to t_0-$. Here the coefficients multiplying the powers of $(t_0 - t)$ are of $O(1)$ while $F_1 = T/2 - C$, $F_2 = T/2 + C$ are functions of x only. The 3/2 and 1/2 powers above follow from a line of reasoning similar to that employed earlier. Also the appropriate scales spatially are given by $x - x_0 = (t_0 - t)^{1/2}\xi$ with the coordinate ξ of being order unity, and $H_1 \sim (t_0 - t)$, specifically

$$H_1 = (t_0 - t)\hat{H}_1(\xi) + \dots \ , \tag{13}$$

where $h_{10} - F_{10} + (x_0 - \frac{1}{2})\theta_{10} = 0$ by definition of a clash; $F_{11} = \theta_{10}$ as slopes cancel; and $\hat{H}_1(\xi) = A + B\xi^2$. The constants A, B are positive. Comparisons with numerical work are shown in figure 4 and these tend to support the trends of (12)–(13) and their immediate consequences.

Substitution into (10a) shows that for consistency the relation

$$c_{11} + (x_0 - \frac{1}{2})h_{11} + \frac{1}{2}(x_0 - \frac{1}{2})^2 \theta_{11} = 0 \tag{14}$$

must hold, together with the expansion

$$u_1 = (t_0 - t)^{-\frac{1}{2}} U_1(\xi) + \dots \tag{15}$$

of the velocity in gap 1. The velocity in gap 2 remains finite, by contrast. The numerical findings in figure 4 tend to support the implication (14). Furthermore from (10a) the velocity coefficient here is given by

$$U_1(\xi) = \frac{\alpha + \beta\xi}{A + B\xi^2} \ , \tag{16}$$

with $\alpha = c_{12} + (3/2)(x_0 - 1/2)h_{12} + (3/4)(x_0 - 1/2)^2\theta_{12}$ and $\beta = h_{11} + (x_0 - 1/2)\theta_{11} = A$, the approach speed of the body, which is given by dH_1/dt evaluated from (13) and is generally positive. From (15) and (5b) we infer that the local pressure expansion in gap 1 must have

$$p_1 = (t_0 - t)^{-1} P_1(\xi) + \dots \ , \tag{17}$$

whereas in gap 2 the pressure $p = p_2$ is substantially smaller. Hence the governing equation

$$\frac{1}{2}U_1 + \frac{\xi}{2}U_1' + U_1 U_1' = -P_1' \tag{18}$$

applies due to (5b). In addition the body movement according to (9) requires

$$\frac{3}{4}Mh_{12} = \int P_1 \ d\xi \ , \tag{19a}$$

$$\frac{3}{4}I\theta_{12} = (x_0 - \frac{1}{2}) \int P_1 \ d\xi \ , \tag{19b}$$

formally, as long as the local contributions to the integrals here are the dominant ones — this needs to be checked later. The major point about (19) at this stage is simply that they appear to fit together in a self-consistent manner.

The scaled pressure term P_1 is $-(\xi/2)U_1 - (1/2)U_1^2 - D_1$ from integration of (18), with the constant of integration D_1 being determined as $-A/(2B)$ to ensure decay at large positive or negative ξ. Hence the local scaled velocity and pressure solutions can be written in the normalised form

$$U_1 = QU_{1b} \ , \ P_1 = \frac{Q^2}{2} P_{1b} \ , \ \alpha = AQ\alpha_b \ , \ \xi = Q\xi_b \ , \tag{20}$$

where where $Q = \sqrt{A/B}$ and

$$U_{1b} = \frac{\xi_b + \alpha_b}{\xi_b^2 + 1} \ , \tag{21a}$$

$$P_{1b} = \frac{1 - \alpha_b(\xi_b^3 + 3\xi_b + \alpha_b)}{(\xi_b^2 + 1)^2} \ . \tag{21b}$$

These are plotted in figure 4 for various values of α_b. Clearly if α_b is zero then the pressure P_{1b} is even in ξ_b, U_{1b} is odd in ξ_b, and the pressure decay is relatively fast (like ξ_b^{-4}) at large ξ_b; also the integral appearing in (19) is then convergent. If, on the other hand, α_b is nonzero, then evenness and oddness of the solutions do not hold, the pressure decay is slower (like ξ_b^{-1}) and the integral in (19) is logarithmically divergent.

The most broadly applying case has α_b being nonzero (and this case is supported by the comparisons presented later in section 5). That corresponds to α being nonzero in general and so the asymptotes acting at large ξ_b values,

$$U_{1b} \sim \xi_b^{-1} + \alpha_b \xi_b^{-2} + \dots \ , \tag{22a}$$

$$P_{1b} \sim -\alpha_b \xi_b^{-1} + O(\xi_b^{-3}) \ , \tag{22b}$$

when combined with the local expressions in (15,17), indicate that the velocity and pressure must have the underlying formation

$$u_1 \sim (x - x_0)^{-1} + \alpha_b (t_0 - t)^{\frac{1}{2}} (x - x_0)^{-2} + \dots \implies u_1 \text{ is } O(1) + O((t_0 - t)^{\frac{1}{2}}) \ , \tag{23a}$$

$$p_1 \sim -\alpha_b (t_0 - t)^{-\frac{1}{2}} (x - x_0)^{-1} + O((t_0 - t)^{\frac{1}{2}}) \implies p_1 \text{ is } O((t_0 - t)^{-\frac{1}{2}}) + O((t_0 - t)^{\frac{1}{2}}) \ , \tag{23b}$$

outside of the local region, *i.e.* where x is of order unity along the majority of the body. These predictions lead into the non-local effects studied in the following section. We observe also here that the contributions from the leading-edge jump conditions and the trailing edge smoothness requirements (4a), (8), respectively, have been negligible in the local analysis so far in contrast with their effects which emerge globally as described in the next section. The background issue of whether the body and fluid velocities are mostly finite at a clash has also still to be addressed.

4 Non-local effects

The non-local or global effects operating over the majority of the body as hinted towards the end of the preceding section contribute more or less equally to the major finite-time clashing behaviour. Their description is distinct generally from the local one above but the two descriptions have to match exactly where overlap occurs.

The appropriate expansions for height, orientation and flux, with the typical x being of order unity, again have the pattern (12a–c) whereas the global F_1 here is simply the smooth prescribed shape function $F_1(x) = T/2 - C$, while $F_2(x) = T/2 + C$. Hence, for x not equal to x_0 now the gap widths H_1, H_2 develop according to

$$H_1 = H_{10} + (t_0 - t)H_{11} + (t_0 - t)^{\frac{3}{2}} H_{12} + \dots \ , \tag{24a}$$

$$H_2 = H_{20} + (t_0 - t)H_{21} + (t_0 - t)^{\frac{3}{2}} H_{22} + \dots \ , \tag{24b}$$

with the dominant terms being

$$H_{10} = h_{10} - F_1(x) + (x - \frac{1}{2})\theta_{10} \ , \tag{25a}$$

$$H_{20} = 1 - h_{10} - F_2(x) - (x - \frac{1}{2})\theta_{10} \ , \tag{25b}$$

which give the two scaled gap widths at the clashing time $t = t_0$. The scaled velocity components in the corresponding two gaps are then of the form

$$u_1 = u_{10}(x) + (t_0 - t)^{\frac{1}{2}} u_{11} + \dots \ , \tag{26a}$$

$$u_2 = u_{20}(x) + (t_0 - t)^{\frac{1}{2}} u_{21} + \dots \ , \tag{26b}$$

where, from substitution into (10a,b) the leading contributions satisfy

$$H_{10} u_{10} = c_{11} + (x - \frac{1}{2})h_{11} + \frac{1}{2}(x - \frac{1}{2})^2 \theta_{11} \ , \tag{27a}$$

$$H_{20} u_{20} = c_{21} - (x - \frac{1}{2})h_{11} - \frac{1}{2}(x - \frac{1}{2})^2 \theta_{11} \ , \tag{27b}$$

and equations governing the higher-order corrections can also be written down readily. Mass conservation as represented by (11) requires here that

$$c_{11} + c_{21} = 1 \ , \tag{28a}$$

$$c_{12} + c_{22} = 0 \ , \tag{28b}$$

and so on for successive terms.

The induced gap pressures as anticipated at the end of section 3 are therefore described by

$$p_1 = (t_0 - t)^{-\frac{1}{2}} p_{10}(x) + p_{11}(x) + \dots \ , \tag{29a}$$

$$p_2 = (t_0 - t)^{-\frac{1}{2}} p_{20}(x) + p_{21}(x) + \dots \ . \tag{29b}$$

The controlling equations (5b) thus yield direct balances between the temporal acceleration forces and the pressure gradients,

$$-\frac{1}{2} u_{11} = -\frac{dp_{10}}{dx} \ , \tag{30a}$$

$$-\frac{1}{2} u_{21} = -\frac{dp_{20}}{dx} \ , \tag{30b}$$

at leading order. The high pressure p_1 produced within gap 1 is just as expected from the conclusion to section 3 but the similarly high pressure p_2 induced within gap 2 is perhaps surprising at first sight but is necessary for consistency on the global scale. The leading- and trailing-edge constraints (4a), (8) here require respectively

$$p_{10}(0) = p_{20}(0) = 0 \ , \tag{31a}$$

$$p_{10}(1) = p_{20}(1) \ . \tag{31b}$$

Finally here the body-movement relations (9a,b) give the global contributions

$$\frac{3}{4} M h_{12} = -\int (p_{20}(x) - p_{10}(x)) \ dx \ , \tag{32a}$$

$$\frac{3}{4} I \theta_{12} = -\int (x - \frac{1}{2})(p_{20}(x) - p_{10}(x)) \ dx \ , \tag{32b}$$

to be viewed in conjunction with those in (19a,b). Comment is postponed to the final section.

5 Comparisons

The comparisons in question are between the analysis of the preceding two sections 3, 4 and the numerical results that were presented in section 2. The aim is to shed extra light where possible on the clashing process. The comparisons are shown in figures 6–9.

Figure 6 shows a check on the prediction (14) of the terminal analysis just prior to a clash. Here gap 1 is that in which the clash occurs or is implied by the numerical results. The quantity tested numerically in the figure as regards gap 1 seems clearly to be passing through zero within a finite time, and in line with (14), while the streamwise position x of the zero point is near $x = x_0 = 0.4$, a value agreeing quite well with results in the earlier figures, for example figure 5.

Velocity profiles u_1, u_2 obtained numerically near termination are highlighted in figure 7(a). Here the u_2 profiles have values very much smaller than those of the u_1 velocity profiles, again immediately prior to a clashing taking place. The trend is as predicted in the analysis specifically in sections 3, 4. Corresponding pressure profiles p_1, p_2 computed for the two gaps are shown in figure 7(b). Again the variations associated with the p_2 profiles are considerably smaller in general than for p_1, in keeping with the overall argument in sections 3, 4.

Figures 8, 9 show other quantities of prime interest for comparison with the touchdown analysis, namely $\theta, h, c_1, \dot{\theta}, \dot{h}, \ddot{\theta}, \ddot{h}$. The message appears to be reasonably affirmative as in the previous results. Here the touchdown analysis of sections 3, 4 suggests that we should be seeing three square roots and two inverse-square roots emerging asymptotically near the termination of the computations as pointed out in the figure. Such is apparently what we do indeed see.

The above comparisons of analytical and computational results seem fairly encouraging altogether for the terminal description put forward in the previous two sections, for the clashing process arising at a finite scaled time.

6 Further comments

Solid-solid impacts and the approach towards such impacts in the presence of surrounding fluid have provided the major focus of the present study, as opposed to the solid-fluid interfacial impacts of [33]. Physical and mathematical understanding of the reasons for approach and the dynamics of the clashing seem inherent in the descriptions in sections 2–5. The clash structure fits together at the algebraic level subject to logarithmic effects being implied by (19a,b) with (32a,b). Increased understanding of subsequent rebounds or bounces from the impact and then quite possibly further multiple clashes is also in prospect depending on the specific contexts and follow-up. On the one hand there is the detailed question of whether the clash in the presence of containing fluid leads simply to a reversal of the approach velocity or not and on the other hand there is the clear suggestion shown by [32] that due to interactive instabilities continual clashing is inevitable in the current settings. The times, scales and orientations at which such clashes continue to take place are governed by the system and typical solutions investigated in the paper. What happens here in the longer run as clashes abound is of much wider concern.

Only a single body has been included so far with thickness or camber or both being significant in the fluid-body interactions. The approach however is readily extendable to more bodies, in fact to any finite number of them and then onward to the large-number (continuum) limit which was addressed in detail in [32] for that particular scenario. This aspect would be interesting to pursue in further work. The issue also of precisely what effect clashes followed by bounces act as or lead on to within the continuum limit is an intriguing one.

Several miscellaneous matters of relevance here also arise, as detailed in the following points. (i) We would expect linear instability to be present as in the earlier Smith-Ellis scenario say for a uniform configuration but this has not yet been investigated in detail. (ii) The extension of the theory to three spatial dimensions would mark a great step forward in understanding. (iii) The parameter range associated with viscous-inviscid interactions as distinct from the inviscid interactions studied herein also poses a significant challenge to the theoreticians. (iv) Another issue surrounds whether anything general can be taken from the results in the sense of clashes, rebounds and then multiple rebounds that involve smooth surfaces; this likewise has still to be addressed fully. (v) The extreme of nearly ballistic motion of the contained body or bodies has been investigated in preliminary work by FTS and Amy Brookes-Beighton. (vi) Interaction results obtained for increasing body thicknesses suggest a subtle changeover can arise at comparatively small values of the thickness in relation to the zero-thickness case of [32]; this is

because of the delay in thickness effects influencing the leading edge region that dominates in the zero-thickness case. (vii) Essentially the same physics and issues arise for the related context of skimming as in [33]; this indicates that there may well be a similar more general description of lift-off holding for the skimming context when rebounds are produced; such solid-fluid impacts lead on, of course, to multiple subsequent skimmings and rebounds.

Acknowledgements

Thanks are due to Roger Gent, Jim Oliver, Sasha Korobkin for their interest and comments at various stages.

References

[1] O.M. Faltinsen. The effect of hydroelasticity on ship slamming. *Phil. Trans. R. Soc. A*, **355**:1–17, 1997.

[2] K. Maki, D.J. Piro, and D Lee. Fluid-structure interaction during ship slamming. Talk at Fifth OpenFOAM Workshop, Gothenburg, Sweden `http://web.student.chalmers.se/groups/ofw5/Presentations/KevinMakiSlidesOFW5.pdf`, 2010.

[3] S.B. Savage. Gravity flow of cohesionless granular materials in chutes and channels. *J. Fluid Mech.*, **92**:53–96, 1979.

[4] F.T. Smith and A.S. Ellis. A continuum model for a chute flow of grains. *SIAM J. Applied Math.*, **69**:305–329, 2008.

[5] G. Luxford, D. Hammond, and P. Ivey. Role of droplet distortion and break-up in large droplet aircraft icing. Presented at the AIAA 42nd Aerospace Sciences Meeting and Exhibition, Reno NV, USA: AIAA-2004-0411, Jan 2004.

[6] R.W. Johnson (ed.). *The Handbook of Fluid Dynamics*. CRC Press, 1998.

[7] E. Stride. Characterisation and design of microbubble-based contrast agents suitable for diagnostic imaging. In E. Quaia, editor, *Contrast Media in Ultrasonography: Basic Principles and Clinical Applications*, pages 31–42. Springer, first edition, 2005.

[8] D.A. Drew. Mathematical modelling of two-phase flow. *Ann. Rev. Fluid Mech.*, **15**:261–291, 1983.

[9] F.T. Smith and R. Purvis. Air effects on droplet impact. Presented at the 4th AIAA Theoretical Fluid Mech Mtg, Toronto, Canada: AIAA-2005-5184, 6–9 Jun 2005.

[10] M. Quero, D.W. Hammond, R. Purvis, and F.T. Smith. Analysis of super-cooled water droplet impact on a thin water layer and ice growth. Presented at the 44th AIAA Aerospace Sci Mtg and Exhibit, Reno Nv, USA: AIAA-2006-466, 9–12 Jan 2006.

[11] D. Gueyffier, J. Li, A. Nadim, R. Scardovelli, and S. Zaleski. Volume-of-fluid interface tracking with smoothed surface stress methods for three-dimensional flows. *J. Comp. Phys.*, **152**:423–456, 1999.

[12] C. Josserand and S. Zaleski. Droplet splashing on a thin liquid film. *Phys. Fluids*, **15**: 1650–1657, 2003.

[13] R. Purvis and F.T. Smith. Air-water interactions near droplet impact. *J. Appl. Math.*, **15**: 853–871, 2004.

[14] R. Purvis and F.T. Smith. Droplet impact on water layers: post-impact analysis and computations. *Phil. Trans. R. Soc. A*, **363**:1209–1221, 2005.

[15] R.G.A. Bowles and F.T. Smith. Lifting multi-blade flows with interaction. *J. Fluid Mech.*, **415**:203–226, 2000.

[16] R. Purvis and F.T. Smith. Planar flow past two or more blades in ground effect. *Q. J. Mech. Appl. Math.*, **57**:137–160, 2004.

[17] H.A. Stone, A.D. Stroock, and A. Ajdari. Engineering flows in small devices: micro-fluidics toward a lab-on-a-chip. *Ann. Rev. Fluid Mech.*, **36**:381–411, 2004.

[18] S.R. Hodges, O.E. Jensen, and J.M. Rallison. The motion of a viscous drop through a cylindrical tube. *J. Fluid Mech.*, **501**:279–301, 2004.

[19] J.A. Schonberg and E.J. Hinch. Inertial migration of a sphere in a Poiseuille flow. *J. Fluid Mech.*, **203**:517–524, 1989.

[20] L. Nikolov and E. Mileva. Neutrally buoyant particle in the boundary layer at a plate. I. Viscous interaction. *Colloid & Polym. Sci.*, **272**:1560–1566, 1994.

[21] R.I. Bowles, N.C. Ovenden, and F.T. Smith. Multi-branching three-dimensional flow with substantial changes in vessel shapes. *J. Fluid Mech.*, **614**:329–354, 2008.

[22] J.K. Comer, C. Kleinstreuer, and C.S. Kim. Flow structures and particle deposition patterns in double-bifurcation airway models. Part 2. Aerosol transport and deposition. *J. Fluid Mech.*, **435**:55–80, 2001.

[23] A. White. *Mathematical modelling of the embolisation process in the treatment of arteriovenous malformations*. PhD dissertation, University of London, 2007.

[24] N.C. Ovenden, F.T. Smith, and G.X. Wu. The effects of nonsymmetry in a branching flow network. *J. Eng. Math.*, **63**:213–239, 2009.

[25] R.I. Bowles, S.C.R. Dennis, R. Purvis, and F.T. Smith. Multi-branching flows from one mother tube to many daughters or to a network. *Phil. Trans. R. Soc. A*, **363**:1045–1055, 2005.

[26] F.T. Smith, L. Li, and G.X. Wu. Air cushioning with a lubrication/inviscid balance. *J. Fluid Mech.*, **482**:291–318, 2003.

[27] F.T. Smith, N.C. Ovenden, and R. Purvis. Industrial and biomedical applications. In G. Meier, K. Sreenivasan, and H.-J. Heinemann, editors, *IUTAM Symposium on One Hundred Years of Boundary Layer Research*, number 129 in Solid Mechanics and its Applications, pages 291–300, 2006.

[28] T.W. Secomb, R. Skalak, N. Özkaya, and J.F. Gross. Flow of axisymmetric red blood cells in narrow capillaries. *J. Fluid Mech.*, **163**:405–423, 1986.

[29] D.P. Gaver III, O.E. Jensen, and D. Halpern. Surfactant and airway liquid flows. In K. Nag, editor, *Lung Surfactant Function and Disorder (Lung Biology in Health and Disease)*, pages 191–227. Taylor & Francis, Boca Raton, Florida, 2005.

[30] J.E.F. Green, F.T. Smith, and N.C. Ovenden. Flow in a multi-branching vessel with compliant walls. *J. Eng. Math.*, **64**:353–365, 2009.

[31] H. Lu, M. Berzins, C.E. Goodyer, P.K. Jimack, and M. Walkley. Adaptive high-order finite element solution of transient elastohydrodynamic lubrication problems. *J. Eng. Tribology*, **220**:215–225, 2006.

[32] F.T. Smith and A.S. Ellis. On interaction between falling bodies and the surrounding fluid. *Mathematika*, **56**:140–168, 2010.

[33] P.D. Hicks and F.T. Smith. Skimming impacts and rebounds on shallow liquid layers. *Proc. R. Soc. A*, in press, 2010.

[34] C.-S. Yih. Fluid mechanics of colliding plates. *Phys. Fluids*, **17**:1936–1940, 1974.

[35] A.A. Korobkin. Impact of two bodies one of which is covered by a thin layer of liquid. *J. Fluid Mech.*, **300**:43–58, 1995.

[36] A.A. Korobkin and M. Ohkusu. Impact of two circular plates one of which is floating on a thin layer of liquid. *J. Eng. Math.*, **50**:343–358, 2004.

[37] J.N. Newman. Analysis of small-aspect-ratio lifting surfaces in ground effect. *J. Fluid Mech.*, **117**:305–314, 1982.

[38] E.O. Tuck. A nonlinear unsteady one-dimensional theory for wings in extreme ground effect. *J. Fluid Mech.*, **98**:33–47, 1980.

[39] A.F. Fortes, D.D. Joseph, and T.S. Lundgren. Nonlinear mechanics of fluidization of beds of spherical particles. *J. Fluid Mech.*, **177**:467–483, 1987.

[40] P.Y. Huang, J. Feng, and D.D. Joseph. The turning couples on an elliptic particle settling in a vertical channel. *J. Fluid Mech.*, **271**:1–16, 1994.

[41] B.H. Yang, J. Wang, D.D. Joseph, H.H. Hu, T.W. Pan, and R. Glowinski. Migration of a sphere in a tube flow. *J. Fluid Mech.*, **540**:109–131, 2005.

[42] A.M. Ardekani, R.H. Rangel, and D.D. Joseph. Motion of a sphere normal to a wall in a second-order fluid. *J. Fluid Mech.*, **587**:163–172, 2007.

Figure captions

Figure 1: Configuration and nomenclature for a single body in the channel. Camber and thickness are exaggerated in these diagrams.

Figure 1(a): The slender body at general position and orientation in the flow. The *chord line*, being the straight line through the leading and trailing edges, makes an angle θ with the x-axis.

Figure 1(b): We define the *mean camber line* $C(x)$ to lie halfway between the upper and lower surfaces of the body, whose separation is given by the *thickness* $T(x)$.

Figure 2: Sample behaviours with only thickness effects present.

Figure 2(a): Here, the body has $C(x) = 0$ and $T(x) = d\sin(\pi x)$ for $d = 0$ (solid lines), $d = 0.2$ (dashed lines), $d = 0.4$ (dotted lines). LHS: body leading edge (LE) and trailing edge (TE) positions. RHS: θ and $\dot{\theta}$.

Figure 2(b): Velocity and pressure profiles at $t = 2$ (well before the clash) for the body with $C(x) = 0$, $T(x) = 0.4\sin(\pi x)$. Solid lines indicate values in gap 1, while dashed lines represent those in gap 2. LHS: Velocities u_1 and u_2. RHS: pressures p_1 and p_2.

Figure 3: Sample behaviours with only camber effects present.

Figure 3(a): Here, the body has $C(x) = -d\sin(\pi x)$ and $T(x) = 0$ for $d = 0$ (solid lines), $d = 0.1$ (dashed lines), $d = 0.2$ (dotted lines). LHS: body leading edge (lowermost line of each d-pair) and trailing edge (uppermost lines) positions. RHS: θ and $\dot{\theta}$.

Figure 3(b): Velocity and pressure profiles at $t = 1$ (well before the clash) for the body with $C(x) = -d\sin(\pi x)$, $T(x) = 0$. Solid lines indicate values in gap 1, while dashed lines represent those in gap 2. LHS: Velocities u_1 and u_2. RHS: pressures p_1 and p_2.

Figure 4: Results (21a,b) for various values of α_b. The two dashed lines in the right-hand figure indicate the predicted large-ξ_b behaviour $P_{1b} \sim \xi_b^{-1}$ (when $\alpha_b = 0$) and $P_{1b} \sim \xi_b^{-4}$ (otherwise).

Figure 5: Gap widths for a body of profile $C(x) = 0$, $T(x) = 0.4\sin(\pi x)$ approaching impact with the lower wall at the scaled time of t about 2.24. Solid lines indicate values in gap 1, while dashed lines represent those in gap 2.

Figure 6: Testing the prediction (14) by plotting numerical values of the right hand sides of (10a,b), for the body of profile $C(x) = 0$, $T(x) = 0.4\sin(\pi x)$. Solid lines indicate values in gap 1, while dashed lines represent those in gap 2.

Figure 7: The numerical behaviour of velocity and pressure approaching the clash. Values in gap 1 are represented by solid lines, those in gap 2 by dashed lines.

Figure 7(a): The velocity u_1 in gap 1 (solid lines) and u_2 in gap 2 (dashed lines) approaching the clash. (The evolution in u_2 is suffiently small over this short time interval that the 11 curves appear to coincide at this plot scale.)

Figure 7(b): The pressure p_1 in gap 1 (solid lines) and p_2 in gap 2 (dashed lines) approaching the clash.

Figure 8: Comparing numerical results with the asymptotic predictions. The three predicted square root asymptotes for $c_1, \dot{\theta}$, and $\dot{h}$ appear to be supported by the numerical results.

Figure 9: Comparing numerical results with the asymptotic predictions. The predicted inverse square root asymptotes appear to be supported by the numerical results.

Short title: Clashing, skimming, bouncing.

Figures

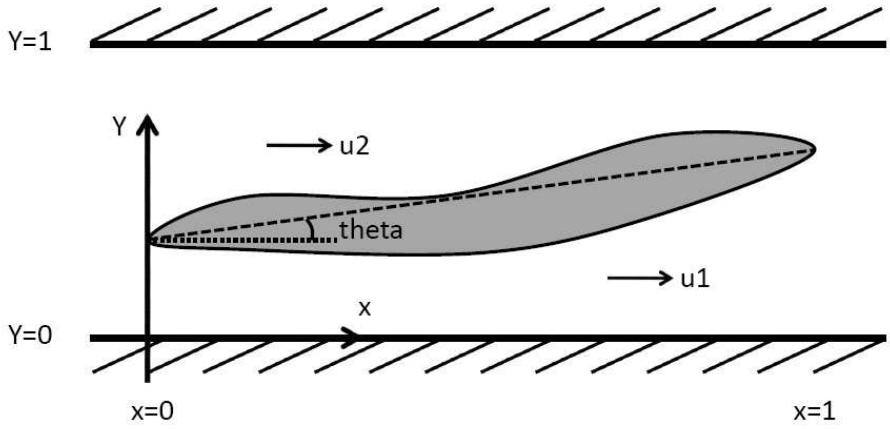

(a) The slender body at general position and orientation in the flow. The *chord line*, being the straight line through the leading and trailing edges, makes an angle θ with the x-axis.

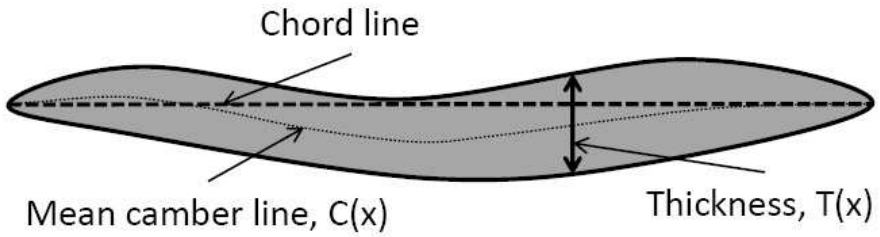

(b) We define the *mean camber line* $C(x)$ to lie halfway between the upper and lower surfaces of the body, whose separation is given by the *thickness* $T(x)$.

Figure 1: Configuration and nomenclature for a single body in the channel. Camber and thickness are exaggerated in these diagrams.

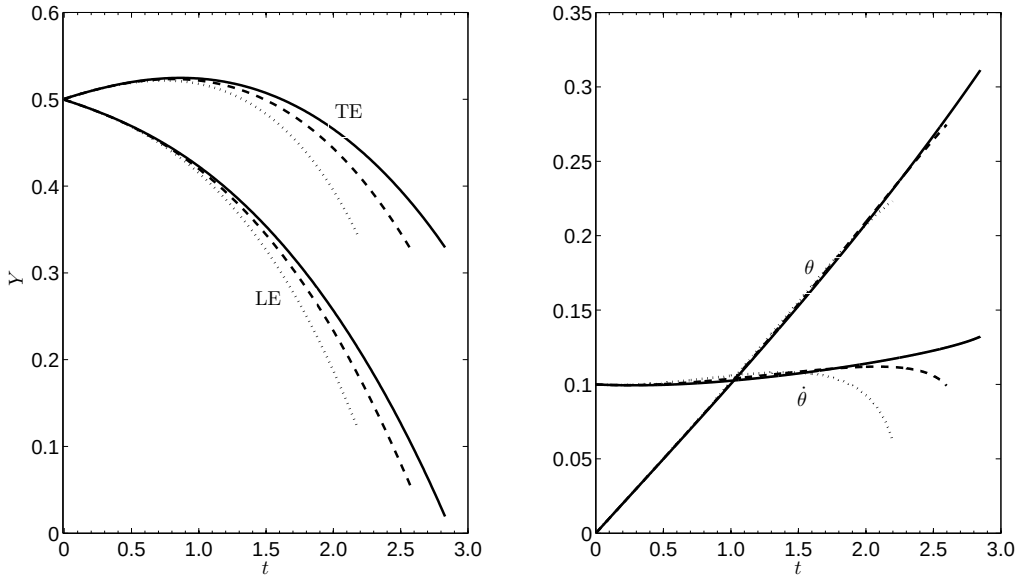

(a) Here, the body has $C(x) = 0$ and $T(x) = d\sin(\pi x)$ for $d = 0$ (solid lines), $d = 0.2$ (dashed lines), $d = 0.4$ (dotted lines). LHS: body leading edge (LE) and trailing edge (TE) positions. RHS: θ and $\dot{\theta}$.

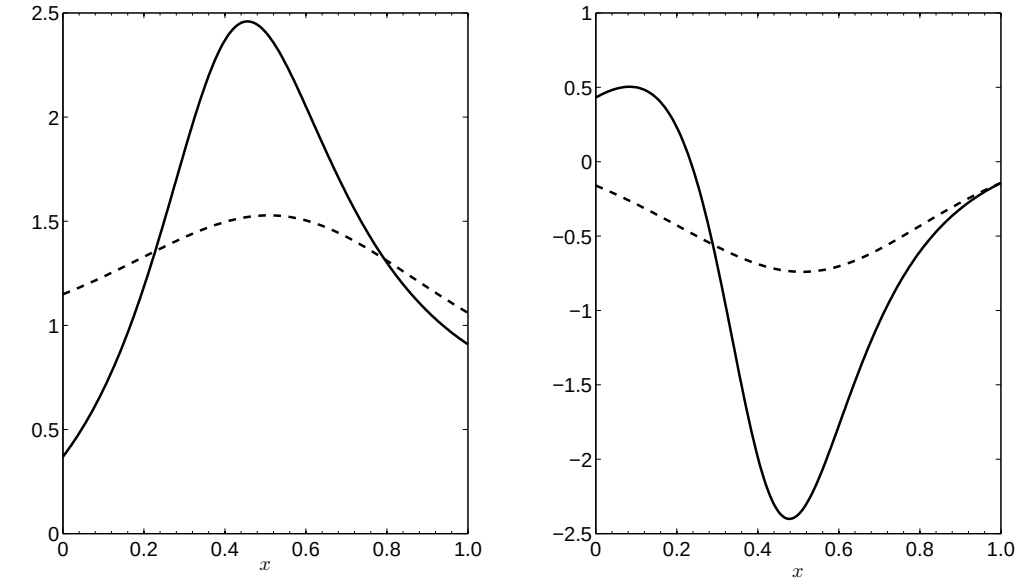

(b) Velocity and pressure profiles at $t = 2$ (well before the clash) for the body with $C(x) = 0$, $T(x) = 0.4\sin(\pi x)$. Solid lines indicate values in gap 1, while dashed lines represent those in gap 2. LHS: Velocities u_1 and u_2. RHS: pressures p_1 and p_2.

Figure 2: Sample behaviours with only thickness effects present.

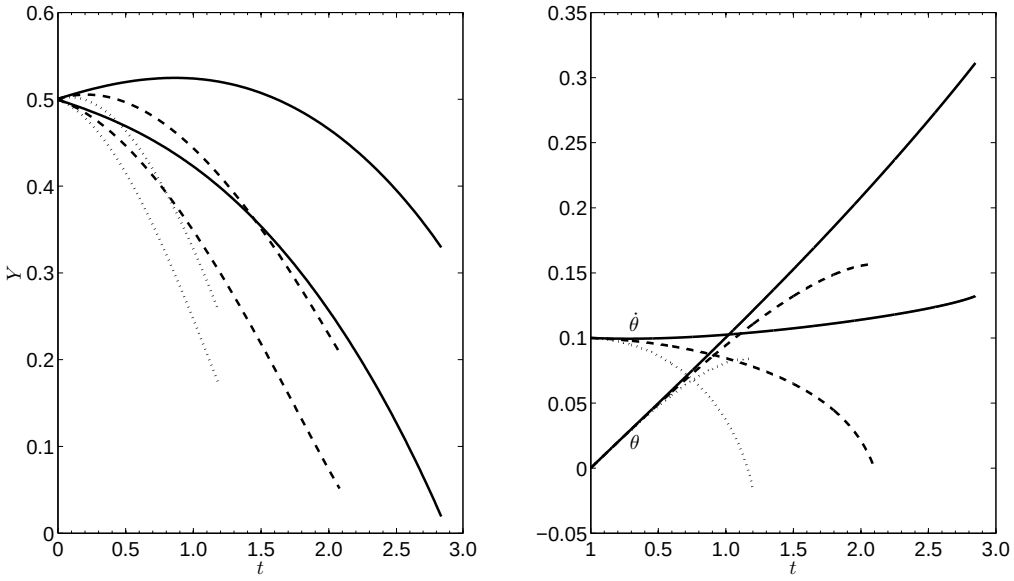

(a) Here, the body has $C(x) = -d\sin(\pi x)$ and $T(x) = 0$ for $d = 0$ (solid lines), $d = 0.1$ (dashed lines), $d = 0.2$ (dotted lines). LHS: body leading edge (lowermost line of each d-pair) and trailing edge (uppermost lines) positions. RHS: θ and $\dot{\theta}$.

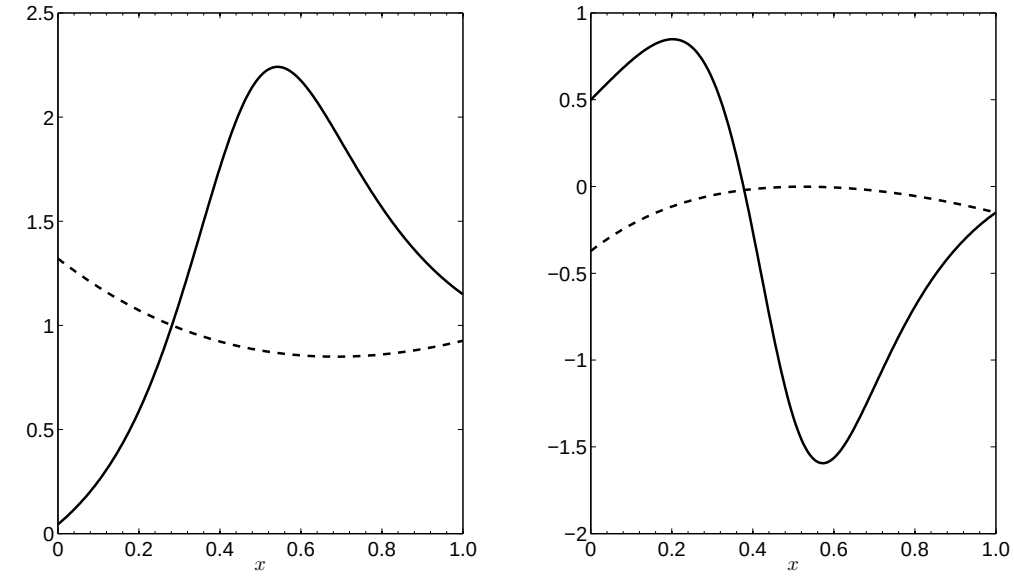

(b) Velocity and pressure profiles at $t = 1$ (well before the clash) for the body with $C(x) = -d\sin(\pi x)$, $T(x) = 0$. Solid lines indicate values in gap 1, while dashed lines represent those in gap 2. LHS: Velocities u_1 and u_2. RHS: pressures p_1 and p_2.

Figure 3: Sample behaviours with only camber effects present.

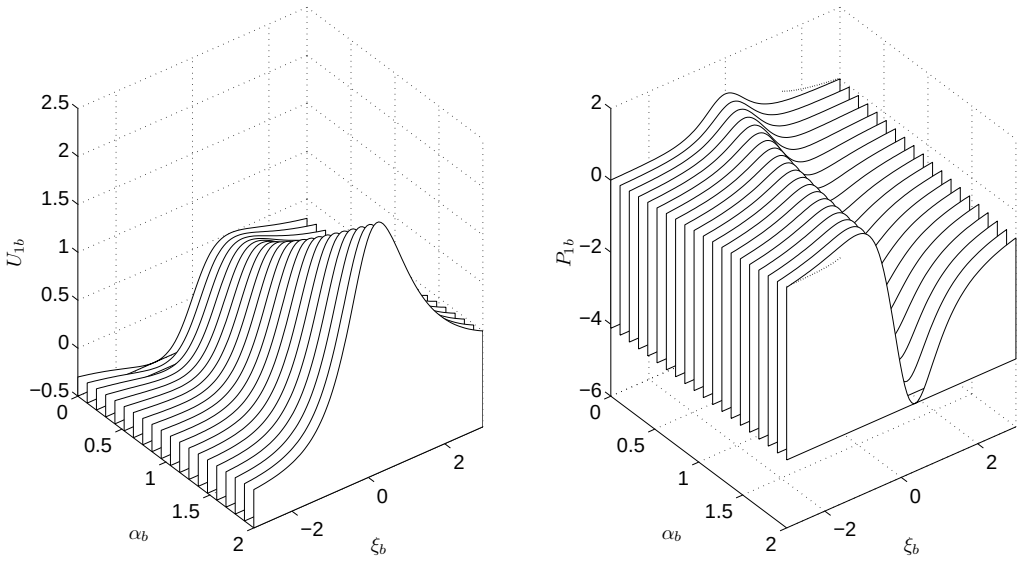

Figure 4: Results (21a,b) for various values of α_b. The two dashed lines in the right-hand figure indicate the predicted large-ξ_b behaviour $P_{1b} \sim \xi_b^{-1}$ (when $\alpha_b = 0$) and $P_{1b} \sim \xi_b^{-4}$ (otherwise).

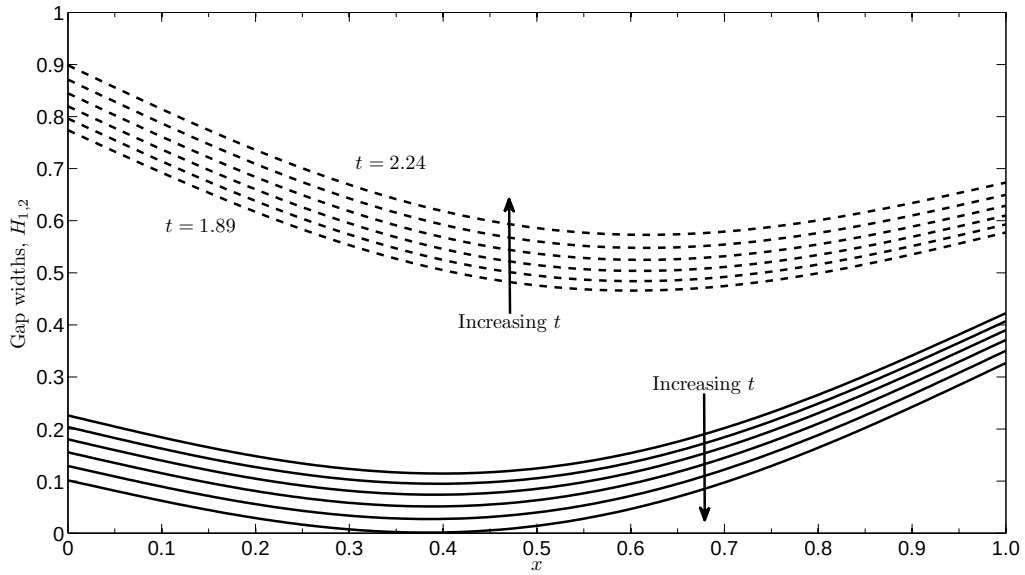

Figure 5: Gap widths for a body of profile $C(x) = 0$, $T(x) = 0.4\sin(\pi x)$ approaching impact with the lower wall at the scaled time of t about 2.24. Solid lines indicate values in gap 1, while dashed lines represent those in gap 2.

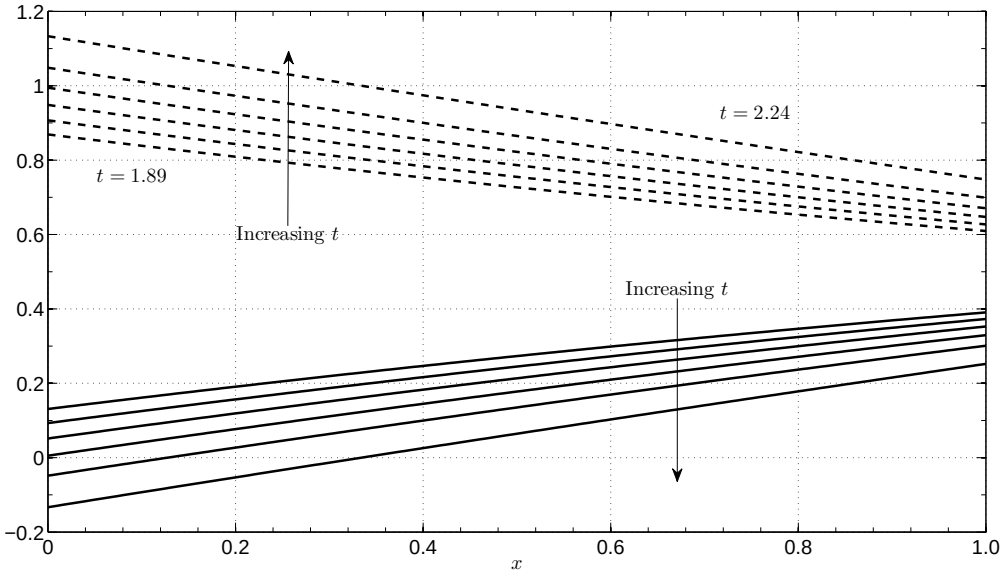

Figure 6: Testing the prediction (14) by plotting numerical values of the right hand sides of (10a,b), for the body of profile $C(x) = 0$, $T(x) = 0.4\sin(\pi x)$. Solid lines indicate values in gap 1, while dashed lines represent those in gap 2.

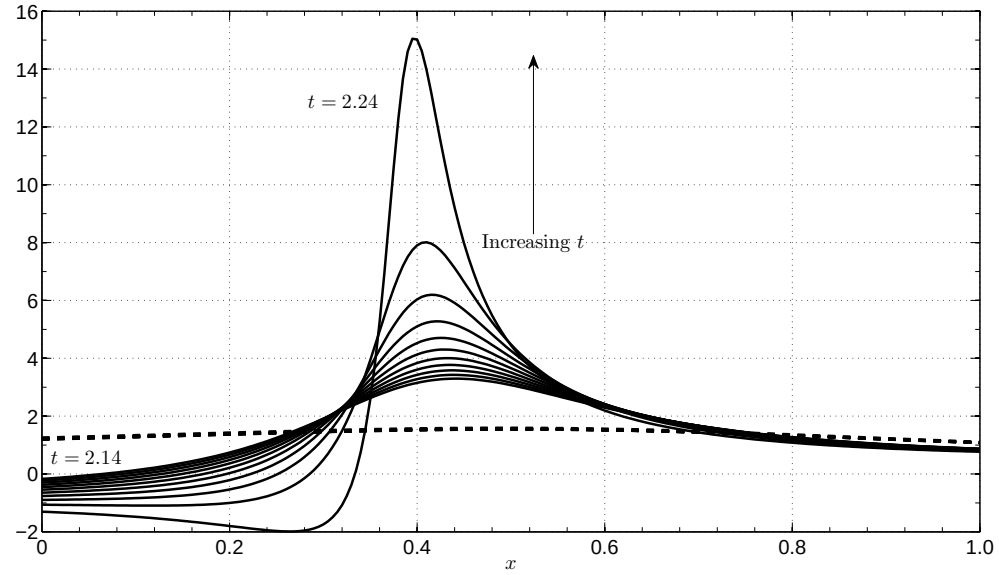

(a) The velocity u_1 in gap 1 (solid lines) and u_2 in gap 2 (dashed lines) approaching the clash. (The evolution in u_2 is suffiently small over this short time interval that the 11 curves appear to coincide at this plot scale.)

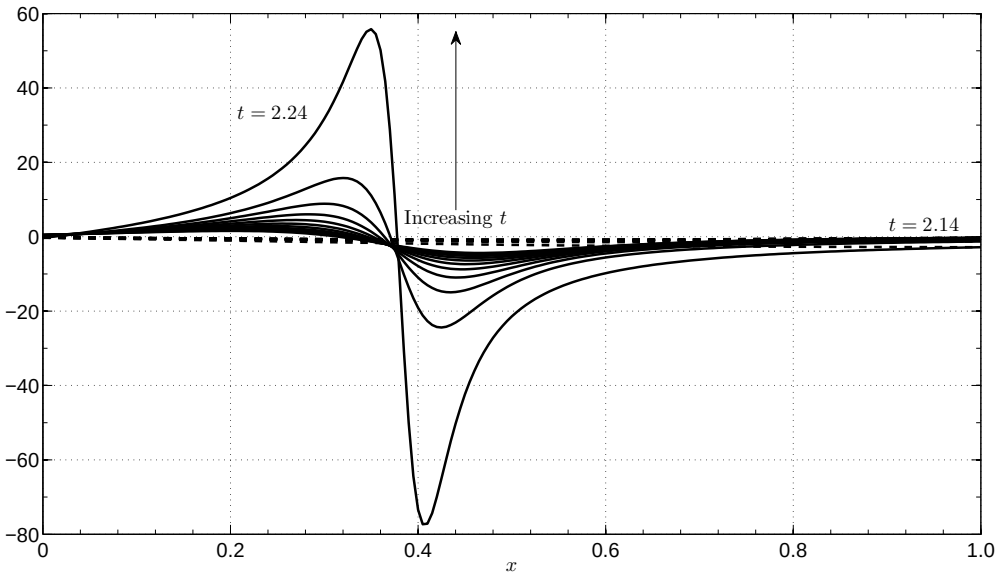

(b) The pressure p_1 in gap 1 (solid lines) and p_2 in gap 2 (dashed lines) approaching the clash.

Figure 7: The numerical behaviour of velocity and pressure approaching the clash. Values in gap 1 are represented by solid lines, those in gap 2 by dashed lines.

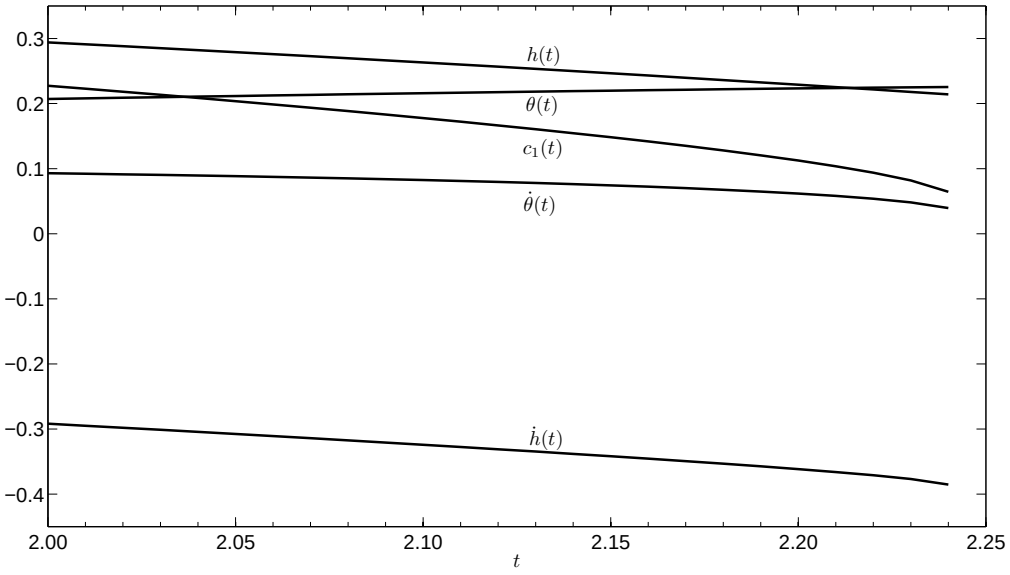

Figure 8: Comparing numerical results with the asymptotic predictions. The three predicted square root asymptotes for $c_1, \dot{\theta}$, and $\dot{h}$ appear to be supported by the numerical results.

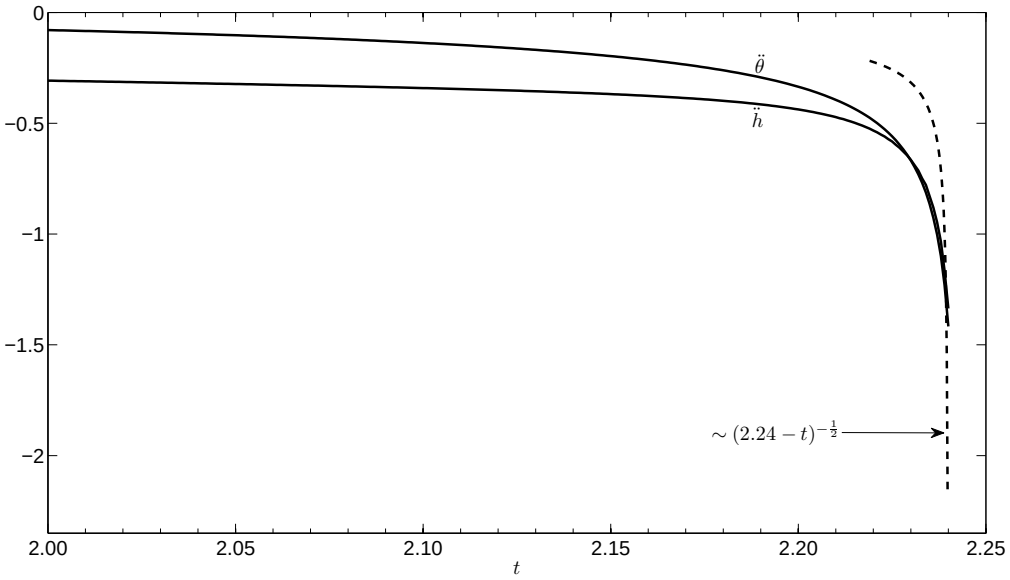

Figure 9: Comparing numerical results with the asymptotic predictions. The predicted inverse square root asymptotes appear to be supported by the numerical results.